Journal of Computational Physics 420 (2020) 109721

Contents lists available at ScienceDirect

Journal of Computational Physics

www.elsevier.com/locate/jcp

Short note

Improving the initial guess for the Newton-Raphson protocol in time-dependent simulations

Jasper C. Volmer [a], Tom W.J. de Geus [b,*], Ron H.J. Peerlings [a]

[a] Department of Mechanical Engineering, Eindhoven University of Technology, P.O. Box 513, 5600 MB Eindhoven, The Netherlands
[b] Institute of Physics, École Polytechnique Fédérale de Lausanne (EPFL), CH-1015 Lausanne, Switzerland

ARTICLE INFO

Article history:
Received 14 December 2019
Received in revised form 10 July 2020
Accepted 13 July 2020
Available online 21 July 2020

Keywords:
Visco-plasticity
Newton-Raphson
Linearisation
FFT solver
Backward Euler

1. Introduction

In simulating real-world problems using quasi-static mechanics, one often models the material's constitutive response using a strain-rate dependent law. One naturally does this when the material possesses a time dependent relaxation mechanism. But it is also common to introduce an artificial strain-rate dependency to regularise numerical solutions of a rate-independent material, e.g. in (crystal) plasticity or damage simulations.

In this setting, we most frequently solve the balance of linear momentum in the following form

$$\nabla \cdot \boldsymbol{\sigma}\left(\boldsymbol{\varepsilon}, \dot{\boldsymbol{\varepsilon}}, t, \ldots\right) = \mathbf{0} \tag{1}$$

i.e. the divergence of the stress $\boldsymbol{\sigma}$ has to vanish everywhere in the domain (see Appendix A for our nomenclature). This problem is generally hard to solve because of the complexity of the stress response at the material point level, as it often depends non-linearly on the strain $\boldsymbol{\varepsilon}$, the strain rate $\dot{\boldsymbol{\varepsilon}}$, the time t, and the loading history (carried in a number of internal variables). This partial differential equation thus has to be solved numerically. To this end, one typically discretises space, resulting in a system of (non-)linear algebraic equations

$$\underline{\boldsymbol{f}}\left\{\underline{\boldsymbol{\sigma}}(\underline{\boldsymbol{\varepsilon}}, \underline{\dot{\boldsymbol{\varepsilon}}}, t, \ldots)\right\} = \underline{\mathbf{0}} \tag{2}$$

where $\underline{f}\{\underline{\bullet}\}$ is a linear or non-linear functional related to the discretisation in space, whereby $\underline{\bullet}$ refers to a discrete set of variables.

* Corresponding author.
E-mail address: tom@geus.me (T.W.J. de Geus).

https://doi.org/10.1016/j.jcp.2020.109721
0021-9991/© 2020 Elsevier Inc. All rights reserved.

By and large, the most popular protocol for solving the system of non-linear equations in Eq. (2) is the Newton-Raphson procedure. This procedure employs a first-order approximation of Eq. (2) in the neighbourhood of an approximate solution $\underline{\boldsymbol{\varepsilon}}_i$, resulting in a linear system of the form

$$\left.\frac{\partial \underline{\boldsymbol{f}}}{\partial \underline{\boldsymbol{\varepsilon}}}\right|_{\underline{\boldsymbol{\varepsilon}}_i} \delta\underline{\boldsymbol{\varepsilon}} = -\underline{\boldsymbol{f}}(\underline{\boldsymbol{\varepsilon}}_i, \ldots) \tag{3}$$

that can be solved for $\delta\underline{\boldsymbol{\varepsilon}}$. The approximate solution is then updated according to

$$\underline{\boldsymbol{\varepsilon}}_{i+1} = \underline{\boldsymbol{\varepsilon}}_i + \delta\underline{\boldsymbol{\varepsilon}} \tag{4}$$

These so-called iterations are repeated until Eq. (2) is satisfied with sufficient precision. In many cases $\underline{\boldsymbol{\sigma}}$ contains ordinary differential equations in time to describe the evolution of the internal variables. These hidden ordinary differential equations are solved by discretising time, often by some finite difference scheme. As a result, Eq. (3) is employed consecutively at different points in time.

The computational efficiency of such a scheme relies crucially on i) the accuracy of the first order approximation in Eq. (3) [1] and ii) the accuracy of the initial guess $\boldsymbol{\varepsilon}_0$ that is iteratively refined using Eq. (4). i) requires a consistent tangent at the material point level and its derivation is usually well established [2–4]. For ii) the obvious choice is to take the last known converged state as the starting point $\boldsymbol{\varepsilon}_0$, however, we show that for time-dependent problems a better choice can be made. It involves a subtle interaction between the non-linear solver and the time dependence. This interaction becomes obvious in the derivation of i) by properly linearising all terms that are part of the discrete time integration scheme. More specifically, we show that a step along the discrete time axis will lead to a viscous flow, regardless of how the system is driven. This is incorporated by an additional stress (or force) term present only in the first iteration after the time increment amending to a logical choice for ii).

The purpose of this note is to present a derivation that naturally leads to the additional term for the first iteration of a new time increment. Furthermore, we show that the additional term can be easily interpreted as an initial guess for the Newton-Raphson protocol. We benchmark the improvement by solving the mechanical response of a dual-phase steel microstructure using a modern numerical method based on the Fast Fourier Transform (FFT) [5–7]. A reduction of the computation time of around 45% is observed in comparison to taking the last known converged state as an initial guess. We emphasise that we present the procedure on a relatively simple model, but that it applies to more complex models as well. We illustrate this by considering also a more involved time integration scheme, and thereby show that the procedure is straightforward to apply.

The remainder of this note is structured as follows: A visco-plastic (time-dependent) material model is introduced together with its linearisation. We thereby distinguish two components: the classical consistent tangent used in every iteration, and an additional driving force inserted during the first iteration. The performance of the classical and improved schemes is examined lastly.

2. Material model

A relatively simple visco-plastic model, based on the small strain assumption, is used here. The employed model is described in [3, chapter 11]. The stress is set by the elastic strain using Hooke's law. Thereto, the total strain $\boldsymbol{\varepsilon}$ is additively split into an elastic part $\boldsymbol{\varepsilon}_e$ and a plastic part $\boldsymbol{\varepsilon}_p$ as

$$\boldsymbol{\varepsilon} \equiv \boldsymbol{\varepsilon}_e + \boldsymbol{\varepsilon}_p \tag{5}$$

and thus

$$\boldsymbol{\sigma} \equiv {}^4\boldsymbol{C}_e : \boldsymbol{\varepsilon}_e \tag{6}$$

with

$${}^4\boldsymbol{C}_e \equiv K\,\boldsymbol{I}\boldsymbol{I} + 2G\,{}^4\boldsymbol{I}^{\boldsymbol{d}} \tag{7}$$

where the fourth-order tensor ${}^4\boldsymbol{I}^d \equiv {}^4\boldsymbol{I}^s - \boldsymbol{I}\boldsymbol{I}/3$ projects an arbitrary tensor $\boldsymbol{A}$ onto its deviatoric part $\boldsymbol{A}^d = \boldsymbol{A} - \mathrm{tr}(\boldsymbol{A})\boldsymbol{I}/3$. The elastic material parameters are the bulk modulus K and the shear modulus G, which depend on Young's modulus E and Poisson's ratio ν in the usual way. The evolution of plastic strain is given by the flow rule as

$$\dot{\boldsymbol{\varepsilon}}_p \equiv \dot{\gamma}\,\boldsymbol{N} \tag{8}$$

whereby the direction of the plastic flow is given by

$$\boldsymbol{N} \equiv \frac{3}{2}\frac{\boldsymbol{\sigma}^d}{\sigma_{eq}} \tag{9}$$

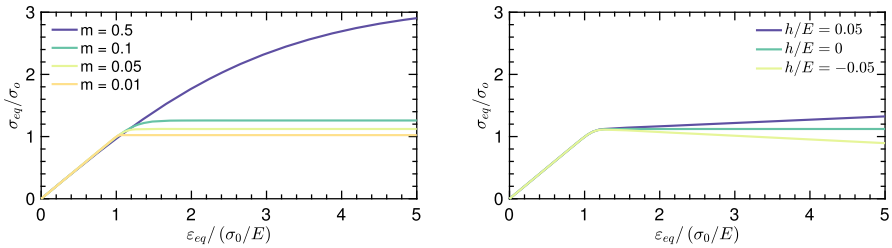

(a) Influence of the rate sensitivity exponent m. (b) Influence of the hardening modulus h.

Fig. 1. Normalised stress-strain curves for an individual visco-plastic material point for $\sigma_0/E = 0.01$ and an applied strain rate of $\dot{\varepsilon}_{eq}/\dot{\gamma}_0 = 10$ in the normal direction. The equivalent strain rate is defined work conjugate to the equivalent stress: $\varepsilon_{eq} \equiv \sqrt{2/3\,\boldsymbol{\varepsilon}^d : \boldsymbol{\varepsilon}^d}$.

where $\boldsymbol{\sigma}^d$ is the deviatoric part of the stress ($\boldsymbol{\sigma}^d = {}^4\boldsymbol{I}^d : \boldsymbol{\sigma}$) and σ_{eq} is the Von Mises equivalent stress ($\sigma_{eq} \equiv \sqrt{3/2\,\boldsymbol{\sigma}^d : \boldsymbol{\sigma}^d}$). The magnitude of the plastic flow $\dot{\gamma}$ is given by Norton's rule as

$$\dot{\gamma} \equiv \dot{\gamma}_0 \left(\frac{\sigma_{eq}}{\sigma_s} \right)^{1/m} \tag{10}$$

The material constants are: the reference strain rate $\dot{\gamma}_0$, the rate-sensitivity exponent m and the yield stress of the material σ_s. Note that $\dot{\gamma}$ is by construction nonnegative, and depends non-linearly on the stress $\boldsymbol{\sigma}$, and therefore on the plastic strain $\boldsymbol{\varepsilon}_p$, through the rate sensitivity exponent m. We, furthermore, let the yield stress σ_s evolve with the accumulated plastic strain as follows:

$$\sigma_s \equiv \sigma_o + h\,\varepsilon_p \tag{11}$$

where σ_0 is the initial yield stress and h is the hardening modulus. If $h = 0$ then the model behaves perfectly plastically, whereas it hardens when $h > 0$ and softens when $h < 0$. Finally, the accumulated plastic strain ε_p is determined from

$$\varepsilon_p \equiv \int_0^t \dot{\gamma}\, dt' \tag{12}$$

To illustrate the behaviour of the visco-plastic model introduced above, several normalised stress-strain curves for a single material point are presented in Fig. 1. Fig. 1a shows the behaviour of the visco-plastic model for several values of the rate sensitivity exponent m. A sharp transition from the elastic to the plastic regime, as would be observed for rate-independent elasto-plastic behaviour, can be approximated by a small value for the rate sensitivity exponent m. The different regimes of hardening, perfect plasticity and softening are shown in Fig. 1b.

3. Time discretisation

The numerical treatment proceeds by discretising the material model in time, for which several choices exist. We employ the implicit Backward Euler protocol, known for its ease of implementation and robust convergence. The procedure is however general, which we demonstrate using the more advanced generalised trapezoidal integration scheme in Appendix C.

Using the Backward Euler protocol, the discrete version of the flow rule in Eq. (8) reads

$$\Delta\boldsymbol{\varepsilon}_p = \Delta\gamma\; \boldsymbol{N}^{t+\Delta t} \tag{13}$$

where

$$\Delta\gamma = \gamma^{t+\Delta t} - \gamma^t = \Delta t\, \dot{\gamma}^{t+\Delta t} \tag{14}$$

To compute the unknowns $\gamma^{t+\Delta t}$ and $\boldsymbol{N}^{t+\Delta t}$, we apply the common approach of performing a radial return map. This involves formulating a trial state ${}^{tr}\bullet$, in which a strain increment is assumed fully elastic, from which the plastic evolution is sought to end up in an admissible state. For a model like the one presented here, this involves solving a single scalar, yet non-linear, equation, as it is easily shown that the stress directions in the trial state are the same as that of the admissible state. We may therefore write $\boldsymbol{N}^{t+\Delta t} = {}^{tr}\boldsymbol{N}$, see e.g. [3] for details.

4. Consistent linearisation of the stress update around an arbitrary reference state

The consistent tangent relates, to the first order, a perturbation in the strain, $\delta\boldsymbol{\varepsilon}$, to the resulting perturbation in the stress, $\delta\boldsymbol{\sigma}$. In this section we derive this tangent from multivariable linearisation around a fully known 'reference state'. The

reference state is left undefined for the moment, but will be clarified below. This approach allows us to clearly identify the terms that are proposed as improvement.

The procedure begins by writing all unknown variables at time $t+\Delta t$ as a fully known reference state $\bullet^*$ plus a small perturbation $\delta\bullet$. In terms of our model we have:

$$\boldsymbol{\sigma}^{t+\Delta t} \equiv \boldsymbol{\sigma}^* + \delta\boldsymbol{\sigma} \tag{15}$$

$$\boldsymbol{\varepsilon}^{t+\Delta t} \equiv \boldsymbol{\varepsilon}^* + \delta\boldsymbol{\varepsilon} \tag{16}$$

$$\boldsymbol{\varepsilon}_p^{t+\Delta t} \equiv \boldsymbol{\varepsilon}_p^* + \delta\boldsymbol{\varepsilon}_p \tag{17}$$

$$\boldsymbol{N}^{t+\Delta t} \equiv \boldsymbol{N}^* + \delta\boldsymbol{N} \tag{18}$$

$$\gamma^{t+\Delta t} \equiv \gamma^* + \delta\gamma \tag{19}$$

$$\dot{\gamma}^{t+\Delta t} \equiv \dot{\gamma}^* + \delta\dot{\gamma} \tag{20}$$

The next step is to linearise all the equations used in the calculation of the constitutive response around the reference state $\bullet^*$. The elastic law in Eq. (6) is already linear and hence gives

$$\delta\boldsymbol{\sigma} = {}^4\boldsymbol{C}_e : \left(\delta\boldsymbol{\varepsilon} - \delta\boldsymbol{\varepsilon}_p\right) \tag{21}$$

A first-order approximation of $\delta\boldsymbol{\varepsilon}_p$ is slightly more involved as it is non-linear and time-dependent. Its derivation starts from Eq. (13) and eventually leads to

$$\delta\boldsymbol{\varepsilon}_p = \delta\gamma\, \boldsymbol{N}^* + \underbrace{\left(\gamma^* - \gamma^{*-\Delta t}\right)}_{\Delta\gamma^*} \delta\boldsymbol{N} \tag{22}$$

Note that $\Delta\gamma^*$ and $\boldsymbol{N}^*$ are known quantities. The derivation continues by developing expressions for $\delta\gamma$ and $\delta\boldsymbol{N}$, to acquire a closed-form expression for the small variation of plastic strain $\delta\boldsymbol{\varepsilon}_p$. To obtain $\delta\boldsymbol{N}$ we use the result from the radial return map, so that $\delta\boldsymbol{N} = \delta({}^{tr}\boldsymbol{N})$. The latter can be entirely evaluated in the trial state, and results in

$$\delta\boldsymbol{N} = \left[\frac{3G}{{}^{tr}\sigma_{eq}^*}{}^4\boldsymbol{I}^d - \frac{2G}{{}^{tr}\sigma_{eq}^*}\boldsymbol{N}^*\boldsymbol{N}^*\right] : \delta\boldsymbol{\varepsilon} \tag{23}$$

To find $\delta\gamma$, we combine the results of Eqs. (14), (19) and (20) into

$$\gamma^* - \gamma^t - \Delta t\dot{\gamma}^* + \delta\gamma - \Delta t\delta\dot{\gamma} = 0 \tag{24}$$

By linearising Eq. (10) around $\bullet^*$, the small variation $\delta\dot{\gamma}$ can be written as

$$\delta\dot{\gamma} = \frac{\partial\dot{\gamma}}{\partial\sigma_{eq}}\delta\sigma_{eq} + \frac{\partial\dot{\gamma}}{\partial\sigma_s}\delta\sigma_s = \frac{\alpha^*}{\Delta t}\left(2\boldsymbol{N}^* : \delta\boldsymbol{\varepsilon} - 3\delta\gamma - \frac{\sigma_{eq}^* h\,\delta\gamma}{\sigma_s^* G}\right), \qquad \alpha^* = \frac{\dot{\gamma}_0 G\Delta t}{m\sigma_s^*}\left(\frac{\sigma_{eq}^*}{\sigma_s^*}\right)^{\frac{1}{m}-1} \tag{25}$$

Thereby we have employed the results of Eqs. (21), (22) and (23).

A closed-form expression for $\delta\gamma$ can now be established by substitution of Eq. (25) in Eq. (24). Substituting that expression for $\delta\gamma$ in Eq. (22) and the resulting expression in Eq. (21) finally gives the consistent linearisation of the stress update, as follows

$$\delta\boldsymbol{\sigma} = {}^4\boldsymbol{C}_{vp}^* : \delta\boldsymbol{\varepsilon} - \frac{G\beta^*}{\alpha^*}\left(\Delta t\dot{\gamma}^* - \gamma^* + \gamma^t\right)\boldsymbol{N}^* \tag{26}$$

where the consistent tangent ${}^4\boldsymbol{C}_{vp}^*$ for the visco-plastic model reads

$${}^4\boldsymbol{C}_{vp}^* = {}^4\boldsymbol{C}_e - 2G\beta^*\boldsymbol{N}^*\boldsymbol{N}^* - \frac{\Delta\gamma^* 4G^2}{{}^{tr}\sigma_{eq}^*}\left[\frac{3}{2}{}^4\boldsymbol{I}^d - \boldsymbol{N}^*\boldsymbol{N}^*\right] \tag{27}$$

and

$$\beta^* = \frac{2\alpha^*}{1 + 3\alpha^* + \frac{\sigma_{eq}^* h}{\sigma_s^* G}\alpha^*} \tag{28}$$

which can be further reorganised[1] to:

[1] It may be helpful to realise that the following identity holds: $\frac{G\beta^*}{\alpha^*} = \kappa^*\left(2G - 3G\beta^*\right)$.

$$\delta\boldsymbol{\sigma} = {}^4\boldsymbol{C}^*_{vp} : \left[\delta\boldsymbol{\varepsilon} - \left(\Delta t\dot{\gamma}^* - \gamma^* + \gamma^t\right)\kappa^*\boldsymbol{N}^*\right] \tag{29}$$

with

$$\kappa^* = \frac{1}{\left(1 + \frac{\sigma^*_{eq}h}{\sigma^*_s G}\alpha^*\right)} \tag{30}$$

Note how the choice of the reference state $\bullet^*$ determines at which state the consistent tangent is evaluated and that it does not affect the expression itself. It does, however, affect the relevance of the second term between brackets in Eq. (29), as we will see next.

5. Reference state

5.1. Recovering the classic Newton-Raphson iteration

We now define the reference state denoted by $\bullet^*$. We first consider 'ordinary' Newton-Raphson iterations within one discrete time step $\bullet^{t+\Delta t}$ as for example in Eq. (4). In this case, an iterative update of the unknown(s) is obtained by linearising around the last known iterative state, denoted by the iteration counter i. In this case, Eq. (29) reduces to the classical [2–4]:

$$\delta\boldsymbol{\sigma} = {}^4\boldsymbol{C}^i_{vp} : \delta\boldsymbol{\varepsilon} \tag{31}$$

where the reference state $\bullet^* \equiv \bullet^i$ at $t + \Delta t$, the latter not being explicitly included in the notation. This result follows from Eq. (29) as $\gamma^* \equiv \gamma^i$ and $\dot{\gamma}^* \equiv \dot{\gamma}^i$. Recognising the discretised strain rate ($\Delta t\dot{\gamma}^i \equiv \gamma^i - \gamma^t$) we thus find the three rightmost terms in Eq. (29) to cancel.

5.2. Obtaining the improved initial guess

For the first iteration of every new time increment, we have to be careful. Commonly, one simply uses the last available tangent as in Eq. (31). This would amend to taking the tangent of the last iteration i of the previous time step (at time t), that resulted in a converged state. We argue that, when taking this converged state as our reference state for linearisation ($\bullet^* \equiv \bullet^t$), an extra term appears in the stress update:

$$\delta\boldsymbol{\sigma} = {}^4\boldsymbol{C}^t_{vp} : \left[\delta\boldsymbol{\varepsilon} - \Delta t\,\dot{\gamma}^t\kappa^t\boldsymbol{N}^t\right] \tag{32}$$

where ${}^4\boldsymbol{C}^t_{vp}$ is the consistent tangent according to Eq. (27) evaluated at the converged state at time t. Note that this result trivially follows from Eq. (29) as $\gamma^* \equiv \gamma^t$ and the two rightmost terms cancel. The extra term in Eq. (32) (cf. Eq. (31)) can be interpreted as the increase in plastic strain $\boldsymbol{\varepsilon}_p$ over the time step Δt as caused by the stress $\boldsymbol{\sigma}$ at time t. Note that the magnitude of this plastic strain increase computed from $\Delta t\,\dot{\gamma}^t$ is scaled with the variable κ^t, which takes into account the effect of the plastic strain increase on the yield stress, i.e. $\kappa^t > 1$ for hardening, $\kappa^t = 1$ for perfect plasticity and $\kappa^t < 1$ for softening. Naturally, this expected increase in plastic strain, based on variables at time t, is only an estimate. As a result, $\delta\boldsymbol{\sigma}$ is only a prediction of the incremental change in stress. This prediction thereby effectively sets an initial guess from which to start the regular Newton-Raphson iterations.

The avid reader may wonder if for the first iteration after a time increment, i.e. the situation described above, it would not simply suffice to use an explicit increment to yield the same result. It is emphasised that interchanging Eq. (14) with an explicit substitute (e.g. Forward Euler) yields: i) a different expression for the consistent tangent ${}^4\boldsymbol{C}^t_{vp}$ in Eq. (32) and ii) no compensation for the change in yield stress as the variable κ^t does not appear.

To conclude, it is emphasised that the extra term in Eq. (32) is a result of the load increment and the time-dependent material model. It is therefore only included in the first iteration after a time increment. In the regime where the plastic flow is negligible ($\underline{\dot{\gamma}}^t \approx 0$) or for rate-independent material models, there is no contribution of the improved initial guess.

6. Case study

To show its relevance, we employ the improved initial guess in a case study. Thereby we make use of a modern numerical solution procedure for micro-mechanical problems, that is based on the Fast Fourier Transform (FFT). As extensively described in [5], like in the Finite Element Method, Eq. (1) is solved in a weak sense. The resulting volume integral is evaluated numerically by introducing nodal unknowns that are distributed on a regular grid (i.e. pixels or voxels). Owing to this choice, they can be interpolated using globally supported trigonometric polynomials. Numerical quadrature then proceeds by evaluating equally weighted quadrature points that coincide with the nodes. The result is a scheme in which essentially local equilibrium equations are coupled by the application of the Fourier transform and its inverse, which can be done using efficient and mature FFT libraries. The details of how the improved initial guess appears in the algorithm proposed by [5] are given in Appendix B.

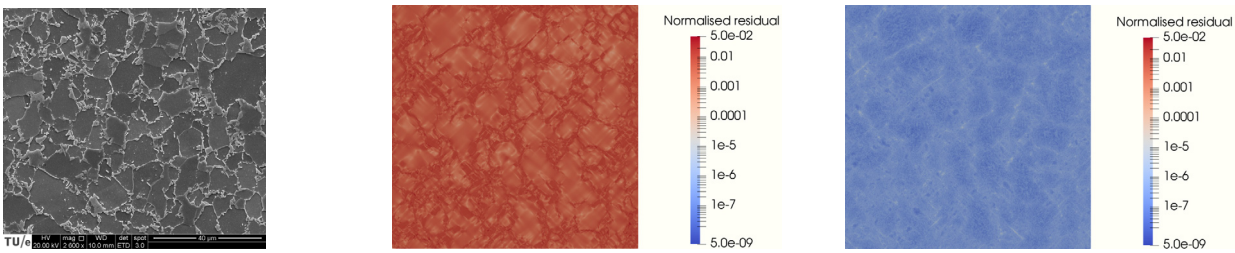

(a) SEM image after scanning. (b) Initial guess as suggested in [5]. (c) Initial guess using the extra term of Eq. (32).

Fig. 2. SEM image (801 x 801 pixels) and visualisation of the magnitude of the residual of the mechanical equilibrium equation normalised with the yield stress of martensite at the start of the Newton-Raphson iterations on the SEM micrograph for perfect visco-plasticity at $\varepsilon_{appl} = 5.0 \cdot 10^{-2}$.

Table 1
Material parameters as assumed for the ferrite and martensite phases.

Parameter	E [GPa]	ν [-]	$\dot{\gamma}_0$ [1/s]	m [-]	σ_0 [MPa]	h [MPa]		
						Hard.	Perf.pl.	Soft.
Ferrite	206.824	0.3	0.001	0.05	425	940	0	-940
Martensite	206.824	0.3	0.001	0.05	1180	1740	0	-1740

We study the efficiency of our improvement based on a realistic example in which we compute the microscopic response of a microstructure that is subjected to a macroscopic shear strain. The microstructure is taken from a micrograph of a commercial dual-phase steel sample (DP600), acquired using a scanning electron microscope (SEM), as shown in Fig. 2a. Dual-phase steel consists of two main constituents: i) ferrite, a soft and ductile phase, which shows up in dark in the micrograph in Fig. 2a and ii) martensite, a hard and brittle phase, which shows up bright in Fig. 2a and has a volume fraction of about 17% in this image of 801x801 pixels. For our case study we assume that the microstructure is continuous and consists only of these two phases, which we both assume to obey the visco-plastic model presented above. To this end the micrograph in Fig. 2a is thresholded[2] to obtain a binary image. Each pixel then corresponds to a nodal point for the FFT-solver, whereby the material parameters are different depending on the phase, see Table 1. Note that we consider three cases: hardening, perfect plasticity, and softening. The parameters for these cases are loosely based on [9] and [10].

In the simulations, the specimen is subject to periodic boundary conditions (as so required by our solver, but common in this type of homogenisation problems). An average strain $\bar{\boldsymbol{\varepsilon}}$ is prescribed which induces a pure shear strain according to

$$\bar{\boldsymbol{\varepsilon}} = \frac{\sqrt{3}}{2}\varepsilon_{appl}\left(\vec{e}_x\vec{e}_x - \vec{e}_y\vec{e}_y\right) \tag{33}$$

where ε_{appl} is the applied strain and $\vec{e}_x$ and $\vec{e}_y$ are the unit vectors, respectively in the horizontal and vertical direction. For the simulations with hardening and perfect plasticity, the applied strain was incrementally increased to $\varepsilon_{appl} = 0.05$ at a strain rate of $\dot{\varepsilon}_{appl} = 0.01$ [1/s] in 100 time steps. For the test cases that include softening, the equivalent strain was incrementally increased to $\varepsilon_{appl} = 0.01$ with the same strain rate and number of time steps.

Figs. 2(b) and 2(c) give an example of the effect of the extra term using the perfectly plastic material model. The residual is visualised based on the computation of the mechanical equilibrium and normalised with the yield stress of martensite. It illustrates how, for this case, the initial guess is nearly perfect if the extra term is employed, while it is quite poor without it. In particular, the relative residuals are as low as 10^{-5} - 10^{-9}, whereas the relative residuals for the initial guess using [5] are in the order of 10^{-2} - 10^{-5}.

The average CPU time used to compute the mechanical response of the microstructure is shown in Fig. 3a. For each considered case, the extra term decreases the CPU time by approximately 45%, by reducing the number of Newton-Raphson iterations per load increment. In particular since the initial guess is closer to the final solution, the convergence of the Newton-Raphson protocol is improved. This is confirmed by the convergence of the relative residual norm in Table 2. As the extra term essentially calculates the increase in plastic strain using the plastic strain rate from the previous time step, it is most accurate where there is little change in plastic strain rate between different time steps, thus especially for the steady

[2] Both the micrograph and the corresponding binary image obtained by thresholding have been taken from the GooseFFT repository [6,7], see [8] for the experimental and thresholding protocol.

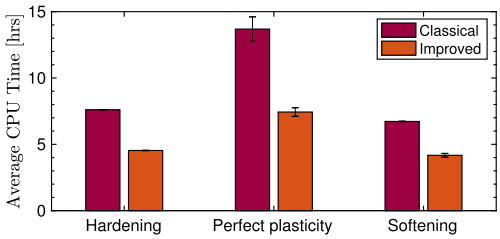

(a) Total CPU time averaged over three runs for different hardening parameters.

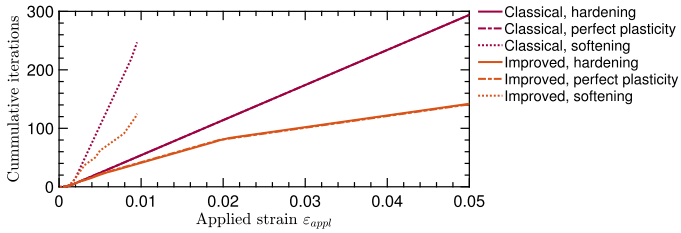

(b) Cumulative number of Newton-Raphson iterations versus applied strain ε_{appl} with overlapping curves for hardening and perfect plasticity.

Fig. 3. Comparison of the numerical performance of the initial guess from [5] (*classical*) and the initial guess from this work (*improved*) for visco-plasticity with hardening, perfect plasticity and softening.

Table 2
Convergence of the norm of the mechanical equilibrium equation normalised with the yield stress of martensite during Newton-Raphson iterations for the classical and improved initial guess, measured at $\varepsilon_{appl} = 0.05$ for the hardening and perfectly plastic case, and at $\varepsilon_{appl} = 0.0075$ for softening, i.e. well in the plastic regime.

Iteration	Hardening		Perfect plasticity		Softening	
	Classical	Improved	Classical	Improved	Classical	Improved
$i = 0$	4.86E+00	5.86E-04	4.64E+00	2.77E-04	3.26E+00	1.42E-03
$i = 1$	1.22E-01	1.49E-08	1.62E-01	1.35E-08	1.36E-01	3.30E-07
$i = 2$	4.96E-04	-	6.87E-04	-	2.02E-03	-
$i = 3$	2.47E-08	-	1.01E-07	-	1.58E-06	-

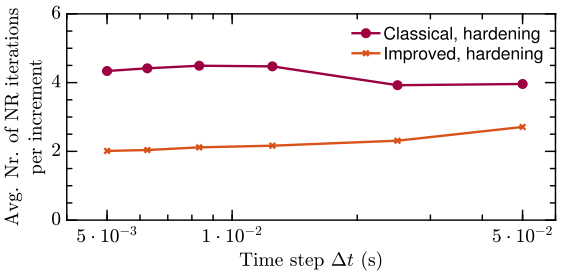

(a) Influence of the time-step Δt.

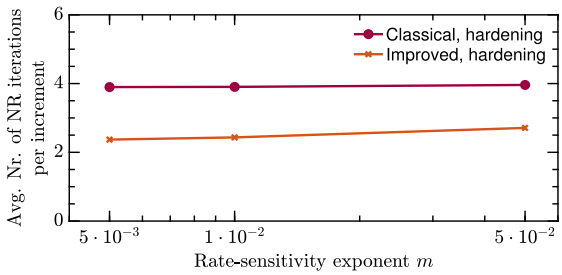

(b) Influence of the rate-sensitivity exponent m.

Fig. 4. Comparison of the average number of Newton-Raphson iterations per time increment of the initial guess from [5] (*classical*) and the initial guess from this work (*improved*) for visco-plasticity with hardening, measured on a 101x101 section of the SEM image of Fig. 2a.

state regime of the perfectly visco-plastic model. This is further illustrated in Fig. 3b, which shows the cumulative number of iterations as a function of the imposed strain. As observed, the improvement becomes clearly visible once the yield stress of the material is reached and the plastic strain starts to develop at a significant rate. For the overlapping curves of the hardening and perfectly plastic case, the effect of the improvement is observable from an applied strain of $\varepsilon_{appl} = 0.005$ onwards. At $\varepsilon_{appl} = 0.02$, the predictability of the plastic strain increases and the improvement distinguishes itself even further. Due to the more localised nature of the plastic strain as the result of softening, the improvement in terms of the number of Newton-Raphson iterations is not monotonic.

When varying the time-step size Δt or the rate-sensitivity exponent m, as shown in Fig. 4, the average number of Newton-Raphson iterations used per load increment is consistently halved by the improvement. Note that the number of time steps was increased with decreasing rate-sensitivity exponent m, such that the ratio between the two was kept constant.

7. Synopsis

A general linearisation procedure for the consistent tangent of a small-strain visco-plastic material model was presented in this note. The procedure is based on multi-variable linearisation around a so-called “reference state”. In particular, the linearisation of the time integration scheme (i.e. Eq. (24)) was found to yield an extra term compared to classical expressions [2–4], which only appears because the material response is time-dependent. It has the effect of yielding a very accurate initial guess for the Newton-Raphson protocol based on the ongoing viscous flow. It was shown, using a modern variational FFT-based solver, that the extra term reduces both the CPU time and the number of Newton-Raphson iterations by around a factor two.

CRediT authorship contribution statement

All authors contributed in the design and execution of the research, and together prepared the manuscript.

Declaration of competing interest

The authors declare that they have no known competing financial interests or personal relationships that could have appeared to influence the work reported in this paper.

Acknowledgement

T.G. was partly financially supported by The Netherlands Organisation for Scientific Research (NWO) by a NWO Rubicon grant number 680-50-1520. J.V. gratefully acknowledges Jan Zeman, Jaroslav Vondřejc and Luv Sharma for their input in discussions concerning FFT-based spectral methods.

Appendix A. Nomenclature

We use boldface symbols to denote vectors $\boldsymbol{a} = a_i \vec{e}_i$, second-order tensors, $\boldsymbol{A} = A_{ij} \vec{e}_i \vec{e}_j$, and fourth-order tensors, ${}^4\boldsymbol{A} = A_{ijkl} \vec{e}_i \vec{e}_j \vec{e}_k \vec{e}_l$. A tensor contraction is denoted using centered dot, e.g. $\boldsymbol{C} = \boldsymbol{A} \cdot \boldsymbol{B}$ corresponds to $C_{ik} = A_{ij} B_{jk}$. A double tensor contraction is denoted using colon, e.g. $c = \boldsymbol{A} : \boldsymbol{B}$ corresponds to $c = A_{ij} B_{ji}$. $\boldsymbol{I} \equiv \delta_{ij} \vec{e}_i \vec{e}_j$ is a second-order unit tensor, and $\boldsymbol{II} \equiv \delta_{ij} \delta_{kl} \vec{e}_i \vec{e}_j \vec{e}_k \vec{e}_l$ corresponds to a dyadic product of two second-order unit tensors. $\mathrm{tr}(\boldsymbol{A}) \equiv A_{ii}/3$ is the trace of second-order tensor. $\nabla \cdot \boldsymbol{A}$ corresponds to the divergence operator $\partial A_{ij}/\partial x_j$. Note that for all index notations a summation of the three spatial dimensions is implied.

Appendix B. Implementation of the improved initial guess

We use Algorithm 1 of Ref. [5] whereby the only modification is line 7 of the algorithm, which now reads

$$\underline{\boldsymbol{G}}\,\underline{\boldsymbol{C}}_{(t)}\,\delta\underline{\boldsymbol{\varepsilon}}^*_{(0)} = -\underline{\boldsymbol{G}}\,\underline{\boldsymbol{C}}_{(t)} \left[\underline{\boldsymbol{E}}_{(t+\Delta t)} - \underline{\boldsymbol{E}}_{(t)} - \Delta t \underline{\dot{\gamma}}^t \underline{\kappa}^t \underline{\boldsymbol{N}}^t\right] \tag{B.1}$$

see Ref. [5] for nomenclature. Here we only specify that we take all nodes (grid-points) visco-plastic and that $\underline{\dot{\gamma}}^t$, $\underline{\kappa}^t$ and $\underline{\boldsymbol{N}}^t$ are columns that collect the nodal quantities. Note also that we use Algorithm 1 of Ref. [5], without any modification, as reference.

Appendix C. Generalised trapezoidal integration

We now generalise our results to the generalised trapezoidal integration scheme, which employs a linear combination of variables evaluated at time t and at time $t + \Delta t$ through a parameter $0 \leq \theta \leq 1$. Note that the choice of this parameter allows one to recover the explicit forward Euler scheme when $\theta = 0$ and the backward Euler scheme when $\theta = 1$. The drawback of the generalised trapezoidal scheme lies in its return map, which requires that the following set of non-linear equations is solved

$$\begin{aligned} \boldsymbol{\varepsilon}_e^{t+\Delta t} &= {}^{tr}\boldsymbol{\varepsilon}_e - \Delta\gamma \left[(1-\theta)\,\boldsymbol{N}^t + \theta \boldsymbol{N}^{t+\Delta t}\right] \\ \Delta\gamma &= \Delta t \left((1-\theta)\,\dot{\gamma}^t + \theta \dot{\gamma}^{t+\Delta t}\right) \end{aligned} \tag{C.1}$$

In comparison, the implicit backward Euler scheme ($\theta = 1$) only requires the solution of the latter, non-linear scalar, equation for $\Delta\gamma$. Using the generalised trapezoidal integration scheme, Eq. (8) is discretised as follows

$$\Delta\boldsymbol{\varepsilon}_p = \Delta\gamma \underbrace{\left((1-\theta)\,\boldsymbol{N}^t + \theta \boldsymbol{N}^{t+\Delta t}\right)}_{\boldsymbol{N}^\theta} \tag{C.2}$$

where

$$\Delta\gamma = \gamma^{t+\Delta t} - \gamma^t = (1-\theta)\,\Delta t \dot{\gamma}^t + \theta \Delta t \dot{\gamma}^{t+\Delta t} \tag{C.3}$$

After linearising Eq. (C.2) around $\bullet^*$, we obtain

$$\delta\boldsymbol{\varepsilon}_p = \delta\gamma\,\boldsymbol{N}^\theta + \underbrace{\left(\gamma^* - \gamma^{*-\Delta t}\right)}_{\Delta\gamma^*}\theta\delta\boldsymbol{N} \tag{C.4}$$

where the quantities $\boldsymbol{N}^\theta$ and $\Delta\gamma^*$ are fully known. The expression for $\delta\boldsymbol{N}$ is derived by linearising its definition in Eq. (9) around $\bullet^*$ as

$$\delta\boldsymbol{N} = \left[\frac{3G}{\sigma^*_{eq}}{}^4\boldsymbol{I}^d - \frac{2G}{\sigma^*_{eq}}\boldsymbol{N}^*\boldsymbol{N}^*\right] : \delta\boldsymbol{\varepsilon}_e \tag{C.5}$$

To find $\delta\gamma$, we combine Eqs. (C.3), (19) and (20) into

$$\gamma^* - \gamma^t - (1-\theta)\,\Delta t\dot{\gamma}^t - \theta\Delta t\dot{\gamma}^* + \delta\gamma - \theta\Delta t\delta\dot{\gamma} = 0 \tag{C.6}$$

The small variation $\delta\dot{\gamma}$ is then derived as

$$\delta\dot{\gamma} = \frac{\partial\dot{\gamma}}{\partial\sigma_{eq}}\delta\sigma_{eq} + \frac{\partial\dot{\gamma}}{\partial\sigma_s}\delta\sigma_s = \frac{\alpha^*}{\Delta t}\left(2\boldsymbol{N}^* : \delta\boldsymbol{\varepsilon}_e - \frac{\sigma^*_{eq}\,h\,\delta\gamma}{\sigma^*_s G}\right), \qquad \alpha^* = \frac{\dot{\gamma}_0 G\Delta t}{m\sigma^*_s}\left(\frac{\sigma^*_{eq}}{\sigma^*_s}\right)^{\frac{1}{m}-1} \tag{C.7}$$

in which α^* is unaffected by the choice of integration scheme. A closed form expression for $\delta\boldsymbol{\varepsilon}_p$ can now be obtained from Eqs. (C.3–C.6). This step of the procedure exposes the major disadvantage of the generalised trapezoidal integration scheme. The lack of co-linearity between ${}^{tr}\boldsymbol{N}$ and $\boldsymbol{N}^*$ requires a system of non-linear equations to be solved during the return map, as opposed to the single non-linear scalar equation for the backward Euler scheme. As a result, both the linearised stress update:

$$\delta\boldsymbol{\sigma} = {}^4\boldsymbol{C}^*_{vp} : \delta\boldsymbol{\varepsilon} - \frac{G\beta^*}{\alpha^*}\left(\theta\Delta t\dot{\gamma}^* + (1-\theta)\,\Delta t\dot{\gamma}^t - \gamma^* + \gamma^t\right)\left({}^4\boldsymbol{P}^*\right)^{-1} : \boldsymbol{N}^\theta \tag{C.8}$$

and the consistent tangent:

$${}^4\boldsymbol{C}^*_{vp} = {}^4\boldsymbol{C}_e - 2G\theta\beta^*\left({}^4\boldsymbol{P}^*\right)^{-1} : \boldsymbol{N}^\theta\boldsymbol{N}^* - \frac{\Delta\gamma^* 4G^2\theta}{\sigma^*_{eq}}\left({}^4\boldsymbol{P}^*\right)^{-1} : \left[\tfrac{3}{2}{}^4\boldsymbol{I}^d - \boldsymbol{N}^*\boldsymbol{N}^*\right] \tag{C.9}$$

contain the inverse of the fourth-order tensor

$${}^4\boldsymbol{P}^* = \left(1 + \frac{3G\theta\Delta\gamma^*}{\sigma^*_{eq}}\right){}^4\boldsymbol{I}^d - \frac{2G\theta\Delta\gamma^*}{\sigma^*_{eq}}\boldsymbol{N}^*\boldsymbol{N}^* \tag{C.10}$$

The constant β^* reads

$$\beta^* = \frac{2\alpha^*}{1 + 2\alpha^*\theta\,\boldsymbol{N}^\theta : \boldsymbol{N}^* + \frac{\sigma^*_{eq}h}{\sigma^*_s G}\theta\alpha^*} \tag{C.11}$$

Note that in the equation above the implicit backward Euler scheme is recovered for $\theta = 1$ as the product $\boldsymbol{N}^\theta : \boldsymbol{N}^* = \frac{3}{2}$ after applying the linearisation as defined in Eq. (18).

Similar to the main text, we have two relevant choices for the reference state $\bullet^*$. An 'ordinary' Newton-Raphson iteration is recovered by taking $\bullet^* \equiv \bullet^i$ at $t + \Delta t$. In this case Eq. (C.8) reduces to the classical

$$\delta\boldsymbol{\sigma} = {}^4\boldsymbol{C}^i_{vp} : \delta\boldsymbol{\varepsilon} \tag{C.12}$$

This result follows from combining the discretised strain rate Eq. (C.3) with Eq. (C.8), cancelling all four terms within brackets in the latter. The improved initial guess is found by taking $\bullet^* \equiv \bullet^t$. In this case $\gamma^* \equiv \gamma^t$ reducing the terms within brackets of Eq. (C.8) to $\Delta t\dot{\gamma}^t$. After some reorganisation, we can write the final result for the stress update in a form identical to the main text, namely

$$\delta\boldsymbol{\sigma} = {}^4\boldsymbol{C}^t_{vp} : \left[\delta\boldsymbol{\varepsilon} - \Delta t\dot{\gamma}^t\kappa^t\boldsymbol{N}^t\right] \tag{C.13}$$

in which the change of integration scheme is only observed by a small change in the constant

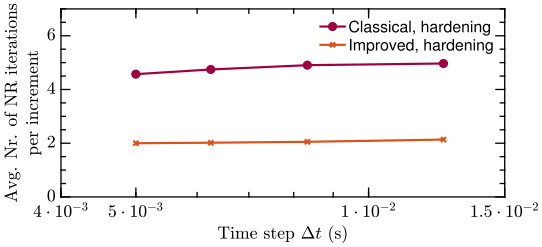

Fig. 5. Comparison of the average number of Newton-Raphson iterations versus the time-step Δt of the initial guess from [5] (*classical*) and the initial guess from this work (*improved*), using visco-plasticity with hardening and the generalised trapezoidal integration scheme with $\theta = 0.5$. These measurements were performed on a 101x101 section of the SEM image of Fig. 2a.

$$\kappa^t = \frac{1}{\left(1 + \frac{\sigma^*_{eq} h}{\sigma^*_s G} \theta \alpha^*\right)} \tag{C.14}$$

Indeed, for $\theta = 1$ Eq. (30) is recovered. Fig. 5 shows the average number of Newton-Raphson iterations used per load increment for different time-step sizes Δt using the trapezoidal scheme with $\theta = 0.5$. The improved initial guess gives results consistent with that of the backward Euler schemes as the Newton-Raphson iterations are approximately halved, saving significant CPU-time.

References

[1] J.C. Simo, R.L. Taylor, Consistent tangent operators for rate-independent elastoplasticity, Comput. Methods Appl. Mech. Eng. 48 (1) (1985) 101–118, https://doi.org/10.1016/0045-7825(85)90070-2.
[2] J.W. Ju, Consistent tangent moduli for a class of viscoplasticity, J. Eng. Mech. 116 (8) (1990) 1764–1779, https://doi.org/10.1061/(ASCE)0733-9399(1990)116:8(1764).
[3] E.A. de Souza Neto, D. Perić, D.R.J. Owen, Computational Methods for Plasticity, John Wiley & Sons, Ltd, ISBN 9780470694626, 2008.
[4] J.C. Simo, T.J.R. Hughes, Computational Inelasticity, Springer-Verlag, ISBN 0-387-97520-9, 1998.
[5] J. Zeman, T.W.J. de Geus, J. Vondřejc, R.H.J. Peerlings, M.G.D. Geers, A finite element perspective on nonlinear FFT-based micromechanical simulations, Int. J. Numer. Methods Eng. 111 (10) (2017) 903–926, https://doi.org/10.1002/nme.5481.
[6] T.W.J. de Geus, J. Vondřejc, GooseFFT, https://github.com/tdegeus/GooseFFT, 2016.
[7] T.W.J. de Geus, J. Vondřejc, J. Zeman, R.H.J. Peerlings, M.G.D. Geers, Finite strain FFT-based non-linear solvers made simple, Comput. Methods Appl. Mech. Eng. 318 (2017) 412–430, https://doi.org/10.1016/j.cma.2016.12.032.
[8] T.W.J. de Geus, J.E.P. van Duuren, R.H.J. Peerlings, M.G.D. Geers, Fracture initiation in multi-phase materials: a statistical characterization of microstructural damage sites, Mater. Sci. Eng. A 673 (2016) 551–556, https://doi.org/10.1016/j.msea.2016.06.082.
[9] X. Sun, K.S. Choi, W.N. Liu, M.A. Khaleel, Predicting failure modes and ductility of dual phase steels using plastic strain localization, Int. J. Plast. 25 (10) (2009) 1888–1909, https://doi.org/10.1016/j.ijplas.2008.12.012.
[10] P. Eisenlohr, M. Diehl, R.A. Lebensohn, F. Roters, A spectral method solution to crystal elasto-viscoplasticity at finite strains, Int. J. Plast. 46 (2013) 37–53, https://doi.org/10.1016/j.ijplas.2012.09.012.